SCIENCE CHINA
Earth Sciences

•RESEARCH PAPER•

October 2022 Vol.65 No.10: 1861–1878
https://doi.org/10.1007/s11430-022-9972-9

Variability of microphysical characteristics in the "21·7" Henan extremely heavy rainfall event

Gang CHEN[1,2,3], Kun ZHAO[2,3*], Yinghui LU[2,3], Yuanyuan ZHENG[1], Ming XUE[2,4], Zhe-Min TAN[2], Xin XU[2], Hao HUANG[2], Haonan CHEN[5], Fen XU[1], Ji YANG[1], Shushi ZHANG[1] & Xueqi FAN[2]

[1] *Key Laboratory of Transportation Meteorology of China Meteorological Administration, Nanjing Joint Institute for Atmospheric Sciences, Nanjing 210041, China;*
[2] *Key Laboratory for Mesoscale Severe Weather/MOE and School of Atmospheric Science, Nanjing University, Nanjing 210023, China;*
[3] *State Key Laboratory of Severe Weather and Joint Center for Atmospheric Radar Research of CMA/NJU, Chinese Academy of Meteorological Sciences, Beijing 100081, China;*
[4] *Center for Analysis and Prediction of Storms and School of Meteorology, University of Oklahoma, Norman, Oklahoma 73072, USA;*
[5] *Colorado State University, Fort Collins, CO 80523, USA*

Received January 28, 2022; revised June 10, 2022; accepted June 20, 2022; published online July 4, 2022

Abstract In this study, significant rainfall microphysical variability is revealed for the extremely heavy rainfall event over Henan Province in July 2021 (the "21·7" Henan EHR event) using a dense network of disdrometers and two polarimetric radars. The broad distributions of specific drop size distribution (DSD) parameters are identified in heavy rainfall from the disdrometer observations, indicating obvious microphysical variability on the surface. A K-means clustering algorithm is adopted to objectively classify the disdrometer datasets into separate groups, and distinct DSD characteristics are found among these heavy rainfall groups. Combined with the supporting microphysical structures obtained through radar observations, comprehensive microphysical features of the DSD groups are derived. An extreme rainfall group is dominantly formed in the deep convection over the plain regions, where the high number of concentrations and large mean sizes of surface raindrops are underpinned by both active ice-phase processes and efficient warm-rain collision-coalescence processes in the vertical direction. Convection located near orographic regions is characterized by restricted ice-phase processes and high coalescence efficiency of liquid hydrometeors, causing the dominant DSD group to comprise negligible large raindrops. Multiple DSD groups can coexist within certain precipitation episodes at the disdrometer stations, indicating the potential microphysical variability during the passage of convective system on the plain regions.

Keywords The "21·7" Henan EHR event, Microphysical characteristics, Variability, Disdrometer, Polarimetric radar

Citation: Chen G, Zhao K, Lu Y, Zheng Y, Xue M, Tan Z M, Xu X, Huang H, Chen H, Xu F, Yang J, Zhang S, Fan X. 2022. Variability of microphysical characteristics in the "21·7" Henan extremely heavy rainfall event. Science China Earth Sciences, 65(10): 1861–1878, https://doi.org/10.1007/s11430-022-9972-9

1. Introduction

In July 2021, an extremely heavy rainfall event occurred in Henan Province, China (the "21·7" Henan EHR event), resulting in destructive floods and huge loss of lives and properties. Majority of precipitation occurred between July 19 and 21, with the average 3-day rainfall accumulation exceeding 300 mm over tens of thousands of square kilometers of the area around Zhengzhou (Figure 1). A record-breaking hourly rainfall of 201.9 mm was observed at the

* Corresponding author (email: zhaokun@nju.edu.cn)

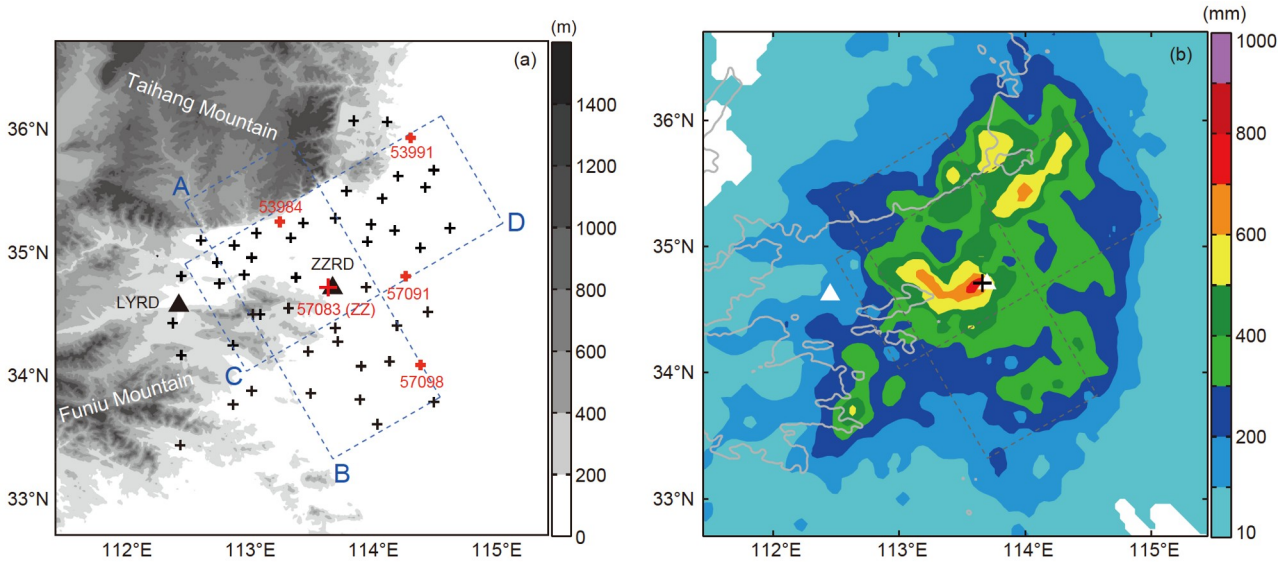

Figure 1 (a) Locations of ground instruments superimposed on the terrain heightmap (gray shadings). Distributions of OTT disdrometers in the national surface stations are represented with black crosses, whereas that of the sites 57083 (ZZ), 53984, 53991, 57091 and 57098 are separately outlined by the crosses (red). The locations of two polarimetric radars (ZZRD, LYRD) are indicated by the two black triangles. Two dashed blue rectangles denote the special investigation areas for the Hovmöller diagrams. (b) Spatial distribution of accumulated precipitation (shading, mm) from July 19 to 21 2021 from the observations of hundreds of gauges (not shown). The 500-m terrain height contours are denoted by gray lines.

Zhengzhou station (ZZ, 57083) on July 20, causing severe urban waterlogging in the city. Previous studies have indicated that surface rainfall intensity is directly reflected in the rain's drop size distribution (DSD), which is determined by the occurrences of microphysical processes in vertical layers (Bringi et al., 2003; Friedrich et al., 2015; Zhang, 2016; Cifelli et al., 2018; Chen et al., 2020; Wen et al., 2020). To reveal the formation mechanism of the "21·7" Henan EHR event, it is crucial to investigate the microphysical characteristics, including surface DSDs and vertical microphysical processes of the heavy rainfall.

Surface DSDs at a given location are commonly obtained from a disdrometer, which measures the number of raindrops in individual size ranges during the passage of a precipitation system (Thompson et al., 2015; Chen et al., 2016; Wen et al., 2016). Recently, precipitation phenomenometers have been widely placed in the national stations of the China Meteorological Administration (CMA); these instruments are inherently disdrometers and record real-time information about DSD. During the abovementioned 3-day period, dozens of this type of disdrometers recorded heavy precipitation DSDs at the national stations. Statistics of surface DSD characteristics in this extreme rainstorm event can be obtained from the observations of the dense network of disdrometers. Moreover, a certain proportion of operational polarimetric Doppler weather radars in China have been upgraded to possess polarimetric capabilities since 2013 (Zhao et al., 2019), including the two in Zhengzhou and Luoyang (ZZRD and LYRD). Information about the species, size, shape, and orientation of hydrometeors in space can be inferred through polarimetric radar observations, which help investigate the occurrences of certain microphysical processes in the vertical direction (Bringi et al., 1986; Vivekanandan et al., 1999; Zhang et al., 2001; Zhao et al., 2019). This extreme rainfall is exactly captured by the two polarimetric radars (ZZRD and LYRD), thereby providing an excellent opportunity to analyze the microphysical structures of the precipitation systems. Based on the combined analysis of disdrometers and polarimetric radars, the relatively comprehensive insights into the microphysical characteristics of rainstorms have been provided (Bringi et al., 2003; Chang et al., 2015; Friedrich et al., 2016; Wang et al., 2016; Wen J et al., 2017; Dolan et al., 2018; Chen et al., 2019; Wen et al., 2020).

Microphysical characteristics vary extensively in different types of precipitation systems. Global convective clusters were first classified into maritime and continental types based on DSD variability and microphysical structures by Bringi et al. (2003), where convection formed in maritime (continental) regions comprises raindrops with smaller (larger) mean sizes and higher (lower) number concentrations. Dolan et al. (2018) and Ryu et al. (2021) reported similar results, where the distinctive type of warm-rain (ice-based) convection causing heavy precipitation mainly exists in the maritime (continental) regions of low (mid) latitudes. Statistical analyses in the low latitude maritime regions have also shown that the convective systems mainly comprise raindrops with high number concentrations and small mean sizes (Thompson et al., 2015; Seela et al., 2017; Zeng et al., 2019; Raut et al., 2021). Additionally, various precipitation microphysical characteristics have been found in different topographic conditions, where relatively deeper (shallower)

convection is easier to form over the plain (orography), causing overall stronger (weaker) ice-phase processes and larger (smaller) surface raindrops (Lang et al., 2009; Luo et al., 2011; Houze, 2012; Xu, 2013; Chang et al., 2015; Cifelli et al., 2018; Zagrodnik et al., 2019). Microphysical variability also exists in specific precipitation cases, where distinct DSD characteristics and related microphysical structures are found in different parts or stages of the convection systems (Wang et al., 2016; Wen J et al., 2017; Wu et al., 2018; Bao et al., 2020; DeHart and Bell, 2020; Han et al., 2021). Radar-derived quantitative precipitation estimation (QPE) relationships are deeply influenced by rainfall microphysical variability, which induces considerable difficulties in obtaining accurate QPE results when using one single relationship (Matrosov et al., 2016; Zhang, 2016; Chen et al., 2017). Moreover, likely, the present bulk microphysics schemes cannot well-reproduce the variability of microphysical characteristics among different rainfall types (Brown et al., 2016; Putnam et al., 2016; Wang et al., 2020; Chen et al., 2021), which possibly restricts the final quantitative precipitation forecast (QPF) performances of the schemes. To improve the QPE and QPF results, a better understanding of microphysical variability is required.

As for summer-time convection in the midlatitude of Eastern Asia, the overall microphysical characteristics are significantly different from the typical continental rainfall but are similar to the maritime convective clusters (Wen et al., 2016; Bang et al., 2020; Wen et al., 2020). Significant microphysical variability also exists in this region for different precipitation systems (Chen et al., 2016; Wen et al., 2018; Chen et al., 2019) or within certain rainfall events (Wen J et al., 2017). For the "21·7" EHR event, heavy rainfall was majorly produced over the foothills of Taihang and Funiu Mountains (Figure 1b), which are complex topographic regions in the midlatitude of Eastern Asia. Abundant water vapor was persistently transported into this region from Typhoon In-Fa at low latitudes, indicating the deep influence of tropic maritime weather systems (Ran et al., 2021). All these conditions offer a great possibility of causing the potential microphysical variability in the record-breaking event. It is worthy of investigating the variability of the precipitation DSDs and vertical structures to comprehensively understand the microphysical characteristics of the rainstorm.

In this study, the microphysical characteristics of the "21·7" EHR event are investigated using the observations of the disdrometer network and polarimetric radar, mainly focusing on the surface DSD variability and vertical microphysical structures. Observed datasets and the adopted DSD clustering algorithm are introduced in Section 2. Properties of DSD groups and the corresponding vertical structure of convection are analyzed in Section 3. The discussion and conclusions are presented in Section 4.

2. Data and methodology

2.1 Surface disdrometers

Surface DSD observations were obtained from a dense network of disdrometers operated by the CMA. Datasets of the OTT Particle Size and Velocity (PARSIVEL) disdrometers located in the national stations of Henan Province (Figure 1a) were collected; 50 OTTs (Figure 1a) with observed rainfall amounts exceeding 200 mm between July 19 and 21 2021, were analyzed in this study. The OTT disdrometers are essentially laser-based optical systems, which produce a horizontal strip of light (1-mm thickness) in a 180-mm long and 30-mm wide measuring area (Löffler-Mang and Joss, 2000). The receiving signal is reduced when hydrometeors fall through the light beam, the amplitude of the signal reduction indicates the particle sizes, and the signal reduction duration determines the fall speeds. OTT measures 32 nonequidistant bins of hydrometeor diameter from 0.062 to 24.5 mm in diameter and 32 bins of fall speeds from 0.05 to 20.8 m s^{-1} (Löffler-Mang and Joss, 2000). Several data quality control (QC) procedures were performed on the OTT datasets to minimize the measurement error: (1) the first two size bins (0.062 and 0.187 mm) were left empty because of the low signal-to-noise ratio, and spurious particles larger than 8 mm were eliminated (Chen et al., 2016); (2) particles outside the ±60% of the fall velocity-diameter relationship (Brandes et al., 2002) were removed to minimize the impact of strong wind or splash in heavy rainfall (Friedrich et al., 2013); (3) 1-min data samples with total drop numbers less than 10 or disdrometer-derived rain rate less than 0.1 mm h^{-1} were also discarded as noise (Chen et al., 2016; Wen L et al., 2017).

After QC, several integral DSD parameters, including the 1-min instant rain rate R (mm h^{-1}), liquid water content LWC (g m^{-3}), and radar reflectivity factor Z (mm^6 m^{-3}) are derived from the obtained raindrop number concentrations in 32 bins, as follows:

$$R = \frac{6\pi}{10^4}\sum_{i=1}^{L} D_i^3 V_i N(D_i)\Delta D_i, \tag{1}$$

$$\mathrm{LWC} = \frac{\pi}{6000}\sum_{i=1}^{L} D_i^3 N(D_i)\Delta D_i, \tag{2}$$

$$Z = \sum_{i=1}^{L} D_i^6 N(D_i)\Delta D_i, \tag{3}$$

where L denotes the total number of raindrop bins for the OTT disdrometer, D_i (mm) denotes the equivalent spherical raindrop diameter, ΔD_i denotes the corresponding diameter interval (mm), V_i (m s^{-1}) denotes the fall speed calculated with the fall velocity-diameter relationship from Brandes et al. (2002), and $N(D_i)$ (mm^{-1} m^{-3}) represents the corresponding number concentration of raindrops for each bin i. Additionally, the log form of the radar reflectivity factor is represented in decibels as Z_H=10log$_{10}$$Z$ (dBZ).

Once the DSD is obtained, the nth-order moment (M_n) of the DSD can be expressed as follows:

$$M_n = \sum_{i=1}^{L} D_i^n N(D_i)\Delta D_i. \quad (4)$$

The mass-weighted mean diameter D_m (mm) is derived as the ratio of the fourth (M_4) to the third moment (M_3) of the DSD:

$$D_m = \frac{M_4}{M_3}. \quad (5)$$

The generalized intercept parameter N_w ($\mathrm{mm^{-1}\ m^{-3}}$) is also computed following Bringi et al. (2003), as follows:

$$N_w = \frac{4^4}{\pi\rho_w}\left(\frac{10^3\mathrm{LWC}}{D_m^4}\right). \quad (6)$$

The specific differential phase K_{DP} (° $\mathrm{km^{-1}}$) is calculated from OTT observations using the T-matrix scattering approach for nonspherical particles (Zhang et al., 2001). Some assumptions in precalculating forward-scattering amplitude $f(0, D)$ (mm) are made: the axis ratio of raindrops is based on Brandes et al. (2002), the raindrop temperature is 20°C, and the canting angle is set to 0°. Then, K_{DP} is obtained as follows:

$$K_{DP} = 10^{-3}\frac{180}{\pi}\lambda Re\left\{\int_{D_{\min}}^{D_{\max}}[f_{hh}(0,D)-f_{vv}(0,D)]N(D)\mathrm{d}D\right\}, \quad (7)$$

where Re denotes the real part of the integral, $f_{hh}(0, D)$ and $f_{vv}(0, D)$ (mm) denote the forward-scattering amplitudes at the horizontal and vertical polarizations, respectively.

Only the 1-min OTT data samples with instant rain rates over 20 $\mathrm{mm\ h^{-1}}$ were selected in the study to analyze the DSD characteristics of heavy precipitation in the "21·7" EHR event, yielding a total of 11,418 heavy rainfall samples for further analysis.

2.2 K-means DSD clustering algorithm

The K-means clustering algorithm was adopted in the study to objectively classify the OTT-observed DSD datasets into separate groups and minimize variability within each DSD group, following Raut et al. (2021). The K-means algorithm is used to objectively group M vectors of N dimensions into k clusters (C_1, C_2,...,C_k), which applies the Euclidean distance as the metric of similarity to minimize the total within-cluster sum of square (d) (Anderberg, 2014; Hartigan and Wong, 1979):

$$d = \sum_{i=1}^{k}\sum_{x\in C_j}|x-\mu_i|^2, \quad (8)$$

where x denotes a vector of N dimensions in cluster C_j, and μ_i denotes the geometric centroid of the vectors in this cluster. In this study, the optimal value of k=5 was determined, the same as in Raut et al. (2021). The length of vectors is equal to the quantity of all selected 1-min OTT samples (M=11,418). For the K-means analysis, we choose the parameters of N_{t1}, N_{t2}, D_m, N_w, and LWC (dimension N=5) to comprehensively describe the DSD characteristics of each 1-min sample, similar to Dolan et al. (2018). N_{t1}(N_{t2}) denotes the total raindrop number concentrations of the first (last) 16 OTT size bins, which represents the overall number concentrations of relatively small (large) raindrops. Because the parameters of N_{t1}, N_{t2}, N_w, and LWC are lognormally distributed (Dolan et al., 2018; Thompson et al., 2015), their log forms [$\log_{10}(N_{t1})$, $\log_{10}(N_{t2})$, $\log_{10}(N_w)$, and $\log_{10}$(LWC)] are used in the clustering algorithm.

Before clustering, five vectors (OTT samples) were randomly selected as the geometric centroids of the clusters. The Euclidean distances for each vector to the five centroids were calculated for the first time, and the corresponding cluster is confirmed (minimum Euclidean distance). After clustering, five groups with a certain quantity of vectors were obtained, and new centroids of each cluster were recalculated. The clustering of groups and calculation of new centroids were repeated as above until all centroids remained unchanged for two successive steps. Following the processing steps of the K-means algorithm, five groups of all selected DSD samples were finally determined.

2.3 Polarimetric radar and additional datasets

Datasets from two S-Pol polarimetric radars (ZZRD and LYRD) covering the OTT network within a 150-km range were collected and analyzed in this study. The two radars possess a range resolution of 250 m and a beamwidth of around 1° and operate at a volume coverage pattern (VCP) mode with nine elevations (0.5°, 1.5°, 2.4°, 3.4°, 4.3°, 6.0°, 9.9°, 14.6°, and 19.5°) every 6 min. Before being used in the study, a QC procedure similar to Huang et al. (2018) was applied. First, nonmeteorological echoes with a correlation coefficient (ρ_{hv}) lower than 0.85 were eliminated (Giangrande and Ryzhkov, 2009). Second, system biases of the differential reflectivity (Z_{DR}) were calibrated using light rain (Z_H from 10 to 20 dBZ) observations (Giangrande and Ryzhkov, 2005), where the averaged Z_{DR} values of the two radars were obtained and compared with the intrinsic Z_{DR} (assumed to be 0 dB) in light rain; thus, differences between the observed and the intrinsic values were considered Z_{DR} system biases. Then, the five-gate median average and running mean were applied to Z_H and Z_{DR}, respectively, to reduce the random fluctuation along the radial axis. Finally, values of the differential phase (Φ_{DP}) were calibrated, unfolded, and smoothed, and the corresponding K_{DP} were recalculated. After QC, the radar datasets of each VCP were interpolated onto a constant altitude plan position indicator (CAPPI) in a Cartesian grid using the NCAR REORDER

software package (available at https://www.eol.ucar.edu/software/reorder). The CAPPI data applied in the study have a 1.0-km horizontal grid spacing and 0.5-km vertical resolution starting from 1.0 to 15 km above ground level (AGL).

We employed a fuzzy-logic hydrometeor identification (HID) algorithm to identify the dominant hydrometeor type in each radar sample volume (Chen et al., 2021; Dolan et al., 2013; Vivekanandan et al., 1999). Five variables—temperature, Z_H, Z_{DR}, K_{DP}, and ρ_{hv}—were selected to calculate the occurrence scores of ten hydrometeor species (drizzle [DZ], rain [RN], big drops [BD], ice crystals [CR], vertical aligned ice [VI], aggregates [AG], wet snow [WS], high-density graupel [HDG], low-density graupel [LDG], and hail [HA]) in each CAPPI grid volume (Dolan et al., 2013). Then, the most likely hydrometeor type to have the highest occurrence score was identified. Although misidentification occasionally occurs due to the inherent uncertainties (e.g., partial overlaps of certain polarimetric radar variable ranges for different hydrometeor types) of the HID algorithm, it is still the most reliable method to obtain the conditions of hydrometeor distributions inside convective systems (Barnes and Houze, 2014; Chen et al., 2019).

Additional data were obtained to help the microphysical analysis in this study. Precipitation amounts from hundreds of automated gauge stations during the 3-day period were collected (Figure 1b). Vertical temperature information was obtained from the radiosonde observations at the ZZ station two times a day. The fifth-generation ECMWF reanalysis (ERA5) hourly data on the 700-hPa level were used to obtain general information on environmental airflows.

3. Results

3.1 Overview of the rainstorm event

During the 3-day period from 08:00 local standard time (LST=UTC+8) July 19 to 08:00 LST July 22, 2021, record-breaking rainfall accumulations occurred over Henan Province (Figure 1b). The observed precipitation was dominantly distributed near the east side of the Tainhang and Funiu Mountains, with the average amount of the 3-day precipitation exceeding 300 mm over a 200-km×200-km area centered around the ZZ station, as indicated by the black cross in Figure 1b. The accumulated precipitation also reached 200 mm over a fraction of upward-sloping terrain regions, as outlined by the 500-m terrain height contours (gray lines). Two obvious heavy precipitation centers are shown in the figure, with the 3-day rainfall exceeding 600 mm; one is exactly located at Zhengzhou; it produced a record-breaking rainfall of 753.9 mm at the ZZ station.

Several studies have described the abnormal synoptic environment during the "21·7" EHR event (Ran et al., 2021; Shi et al., 2021; Su et al., 2021; Yin et al., 2021; Zhang et al., 2021)—that the combination of the northern lifting of the western Pacific subtropical high and the landing of Typhoon In-Fa provided a stable channel to constantly transport water vapor over the continental regions. Additionally, a low-level vortex developed over Henan Province—the southerly airflow of the vortex strengthened the low-level jet and caused the development of precipitation systems (Ran et al., 2021; Su et al., 2021). With the movements of Typhoon In-Fa and the low-level vortex, the locations and intensities of the precipitation systems changed. To analyze the specific spatial and temporal distribution of the precipitation systems during the 3-day period, the Hovmöller diagrams of radar reflectivity in two chosen areas along intersecting directions during the 3-day period are shown in Figure 2. The two slender rectangular areas are marked with dashed boxes in Figure 1; one distributes from the edge of Taihang Mountain to the plain regions in the southeast, and the other covers the two heavy precipitation centers from southwest to northeast. The mean values of 2-km-AGL radar reflectivity in each radar VCP along the short sides of the rectangles are first calculated, and the time series of the averaged Z_H along the long sides are presented with colored contour fillings in Figure 2a1 and 2b1. Regions where the maximum reflectivity exceeds 30 dBZ at 9-km AGL (the −20°C level) are also outlined by gray contours to represent the occurrence of deep convection (Markowski and Richardson, 2010). The mean elevations along the rectangles' long sides are also shown in the top panels (a2, b2). Time series of the domain-averaged wind components along the A-B and C-D directions at 700 hPa level are presented in the right panels (respectively a3 and b3) to provide the general information on environmental airflows.

Several rainfall episodes are found over the 3-day period, as shown by the areas with a mean radar reflectivity of over 34 dBZ (Figure 2). Wide areas of reflectivity exceeding 34 dBZ existed along both directions (A-B and C-D) from 04:00 to 20:00 LST July 20, corresponding to the precipitation systems causing extreme rainfall over Henan Province. Precipitation systems persistently develop and move from the plain regions (B) to the orographic side (A), which agrees with the wind components from B to A (Figure 2a). The moving speed of the rainfall systems is probably dominated by the environmental wind conditions, and higher wind components along the A-B direction contribute to faster movement of the precipitation echoes. The convective systems continuously moved toward the orographic regions from 04:00 to 14:00 LST (Figure 2a1), and appeared to be quasistationary between 14:00 and 20:00 around the ZZ station (the black line). Deep convection was also observed and maintained over Zhengzhou, bringing the record-breaking rainfall up to 201.9 mm h^{-1} (from 16:00 to 17:00 LST July 20) at the ZZ station. Moreover, areas of pre-

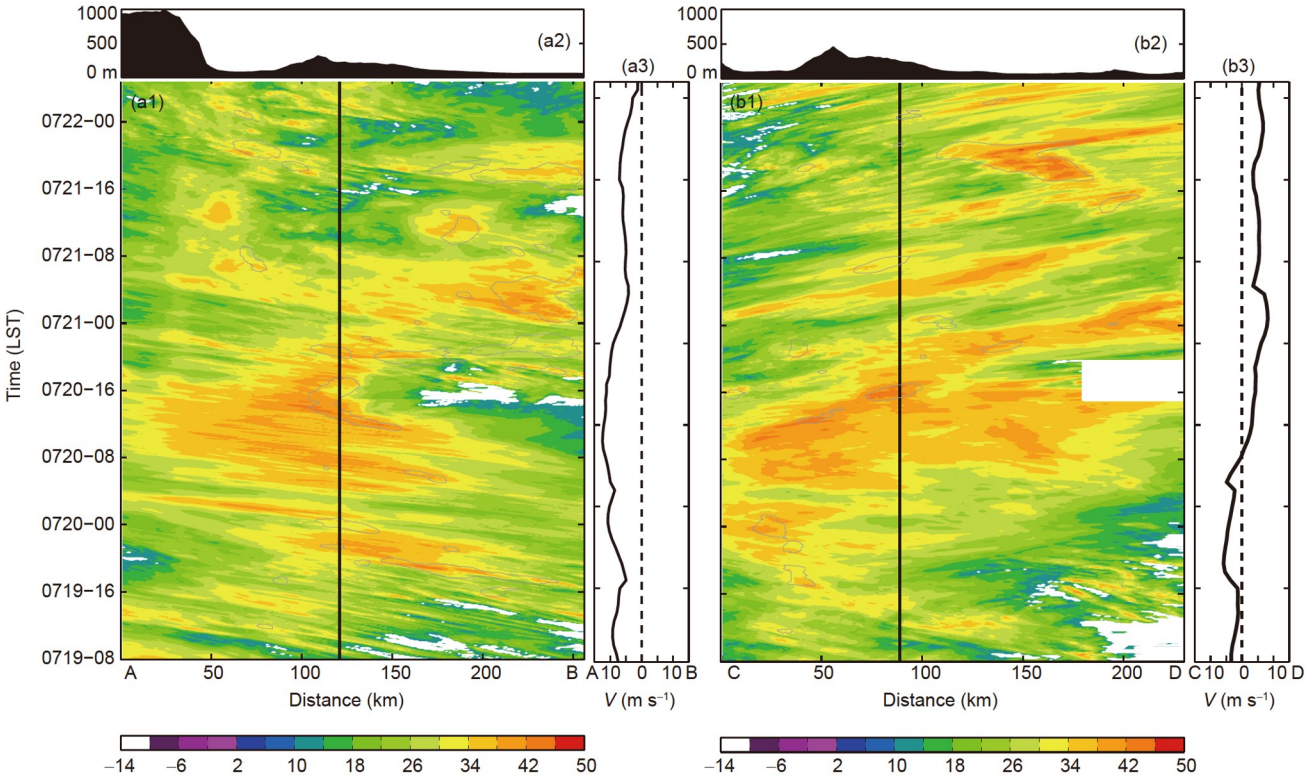

Figure 2 Hovmöller diagram of average reflectivity at 2-km AGL for the slender rectangular areas of (a1) A-B and (b1) C-D shown in Figure 1. The gray contours denote the maximum 30-dBZ reflectivity at 9-km AGL (the −20°C level). Black filling areas in the top panels (a2, b2) indicate the mean surface elevations. Time series of domain-averaged wind components along the A-B and C-D directions from ERA5 hourly reanalysis datasets at 700 hPa level are shown in the right panels (a3 and b3), respectively.

cipitation echoes exceeding 30 dBZ at the −20°C levels were mainly distributed away from the orographic regions, indicating the relatively shallower convection over the upward-sloping terrains. Moreover, a shift of wind components occurred around 08:00 LST on July 20 along the C-D direction parallel to the edge of Taihang Mountain, and the movement directions of precipitation echoes changed accordingly (Figure 2b). Three obvious precipitation episodes also existed along this direction; one persistently produced intense rainfall from Song Mountain (in the middle of LYRD and ZZRD, not shown) to the northeast of Zhengzhou between 04:00 LST July 20 and 04:00 LST July 21, which was exactly the convective system causing extreme precipitation and severe urban waterlogging. The other two episodes, particularly the one composed of deep convection from 16:00 LST July 21 to 00:00 LST July 22, were mainly distributed in the northeast of Zhengzhou and brought extreme rainfall accumulations there.

A total of 56 national surface stations received the accumulated precipitation of over 200 mm during the 3-day period, with hundreds of short-duration heavy precipitation (SDHP, hourly precipitation over 20 mm) hours (Figure 3a). Precipitation reached the maximum value of 201.9 mm h^{-1} at the ZZ station and exceeded 50 mm h^{-1} for dozens of hourly samples. Datasets from 50 OTT disdrometers located among these national stations were collected and analyzed in the study, and DSD characteristics of heavy rainfall were captured by the dense network of disdrometers. Comparison of SDHP hourly rainfall totals between gauges and OTTs at the 50 national stations are also given (Figure 3b), where hourly rainfall totals for disdrometers are averaged from the 1-min rain rates calculated from eq. (1). We use gauge rainfall as ground truth; the correlation coefficient (CC) equals 0.93 for all SDHP samples, and the root mean square error (RMSE) is 7.66 mm, indicating the overall agreement between the two types of observations. The consistency of rainfall also implies the general reliability of DSD observations from the OTT network.

3.2 Variability of overall DSDs

The time series of the raindrop $N(D)$ (m^{-3} mm^{-1}) for five selected OTT sites with heavy rainfall recorded are shown in Figure 4a–4e. Persistent rainfall was observed at site 53984, but almost no raindrop with a size larger than 4 mm (large raindrops) was recorded from July 20 to 21, and values of D_m were lower than 2 mm. As for the other four OTTs, obvious precipitation episodes are observed during the passage of convective systems. A certain number of large raindrops were recorded and high number concentrations (above

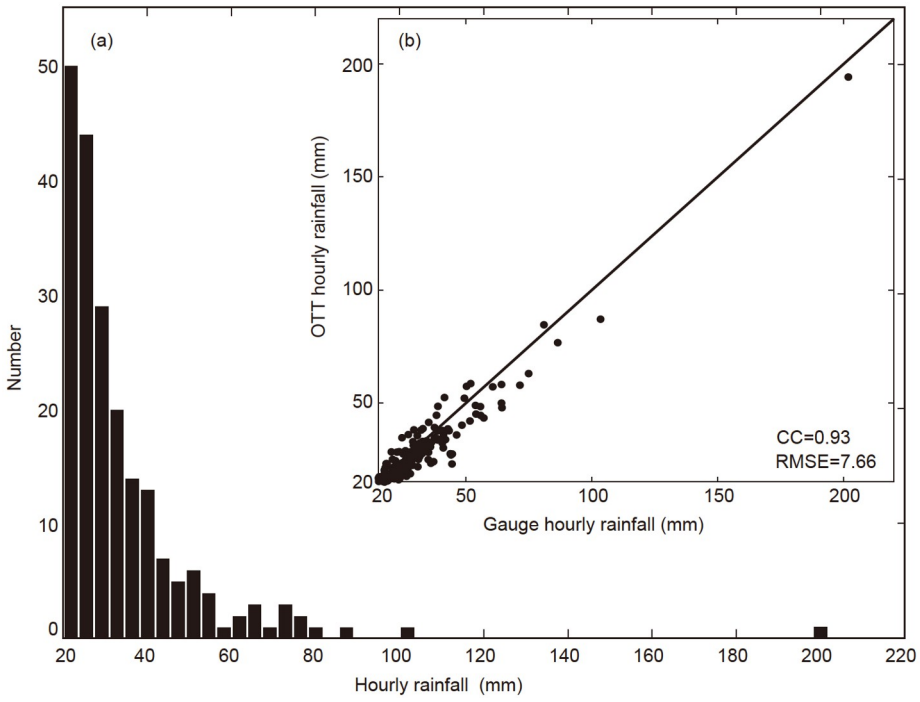

Figure 3 (a) Histogram of SDHP hours from rain gauges in the national stations. (b) Comparison of SDHP hourly rainfall totals between gauges and OTTs, values of CC and RMSE are also given.

10^3 m^{-3} mm^{-1}) of small raindrops (D<2 mm) were observed at each episode, with the maximum D_m around 3 mm. One significant precipitation episode was observed between 15:00 and 18:00 LST on July 20 at the ZZ station (Figure 4c, 57083), with a record-breaking hourly rainfall of 201.9 mm h^{-1}. Extremely high number concentrations of small raindrops (around 10^4 m^{-3} mm^{-1}) were recorded, and the maximum raindrop sizes exceeded 6 mm. Considerable raindrop numbers in nearly all bin sizes contributed to the extreme rainfall.

The joint D-$\log_{10}[N(D)]$ normalized frequency distributions for all OTT 1-min heavy rainfall samples are presented in Figure 4f. The maximum values of $N(D)$ existed when the raindrop diameters were close to 0.6 mm, with the mean value around 10^3 m^{-3} mm^{-1}. Nevertheless, the upper and lower thresholds for raindrops around 0.6 mm were $10^{3.5}$ and $10^{2.5}$ m^{-3} mm^{-1}, respectively, when the normalized frequency was greater than 5%, indicating the variability of maximum raindrop number concentrations by almost an order of magnitude. These dispersions of $N(D)$ were nearly unchanged for small raindrops, whereas they gradually grew for greater raindrop diameters. The upper and lower values of $N(D)$ became 10^2 and 10^0 m^{-3} mm^{-1} for raindrops around 3 mm when the normalized frequency was greater than 5%. Moreover, raindrop diameters changed between 3.0 and 5.5 mm when values of $N(D)$ gradually reduced to 10^0 m^{-3} mm^{-1}. Remarkable dispersions of $N(D)$ for the middle (2–4 mm) and large raindrops (D>4 mm) mainly caused the DSD variability in the "21·7" EHR event.

Significant OTT-observed DSD variability also exists from the distributions of D_m versus $\log_{10}(N_w)$, as presented in Figure 4g. The typical maritime and continental convective clusters reported by Bringi et al. (2003) are shown with separate gray rectangles. For samples with rain rates within 20–50 mm h^{-1} (blue dots), the corresponding values of D_m vary from 1.0 to 3.5 mm and $\log_{10}(N_w)$ from 4.5 to 2.5. Dispersed samples are located from the typical maritime convective cluster area to the continental one. As the increase in instant rain rates (50–100 and over 100 mm h^{-1}), the scatterplots (yellow and red) gradually shift to the upper-right side of the D_m-$\log_{10}(N_w)$ space, whereas the dispersion nearly remains unchanged. Large deviations for both D_m and $\log_{10}(N_w)$ are also indicated by the long crossed black error bars, and the mean of D_m and $\log_{10}(N_w)$ distributes in the middle of the two typical convective boxes. In summary, obvious DSD variability is found in the "21·7" EHR event from the OTT observations, suggesting the complex microphysical characteristics at the surface.

3.3 Clustered DSD comparison

To analyze the sources of the DSD variability, the OTT-observed heavy rainfall samples were further clustered into five groups using the K-means algorithm (Figure 5). A small fraction of the heavy rainfall samples (3%) were clustered into group1 (red), which is characterized by the extremely high raindrop number concentrations for all raindrop size intervals (Figure 5a). The maximum value of $N(D)$ reached

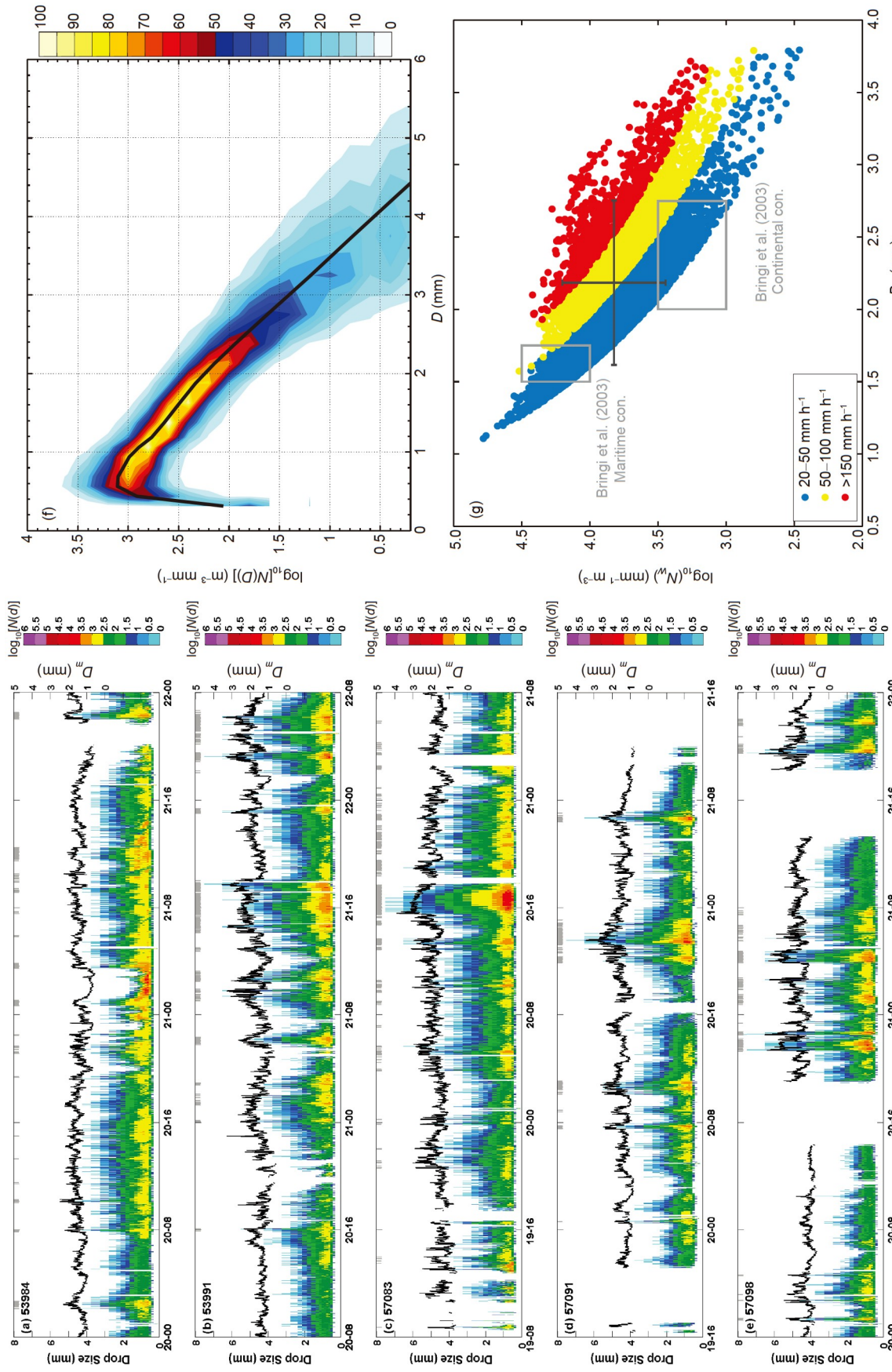

Figure 4 (a)–(e) Time series of the raindrop $N(D)$ (m^{-3} mm^{-1}) for selected OTT sites, the black lines indicate the evolutions of D_m (mm). (f) Joint D-$\log_{10}[N(D)]$ normalized frequency distributions, the colored shadings represent the normalized occurrence frequency of all 1-min DSD samples from 5% to 100%; the black line denotes the mean raindrop size spectra. (g) D_m-$\log_{10}(N_w)$ scatterplots of all 1-min DSD samples, the ranges of deviations for both D_m and $\log_{10}(N_w)$ are also outlined by the crossed black error bars.

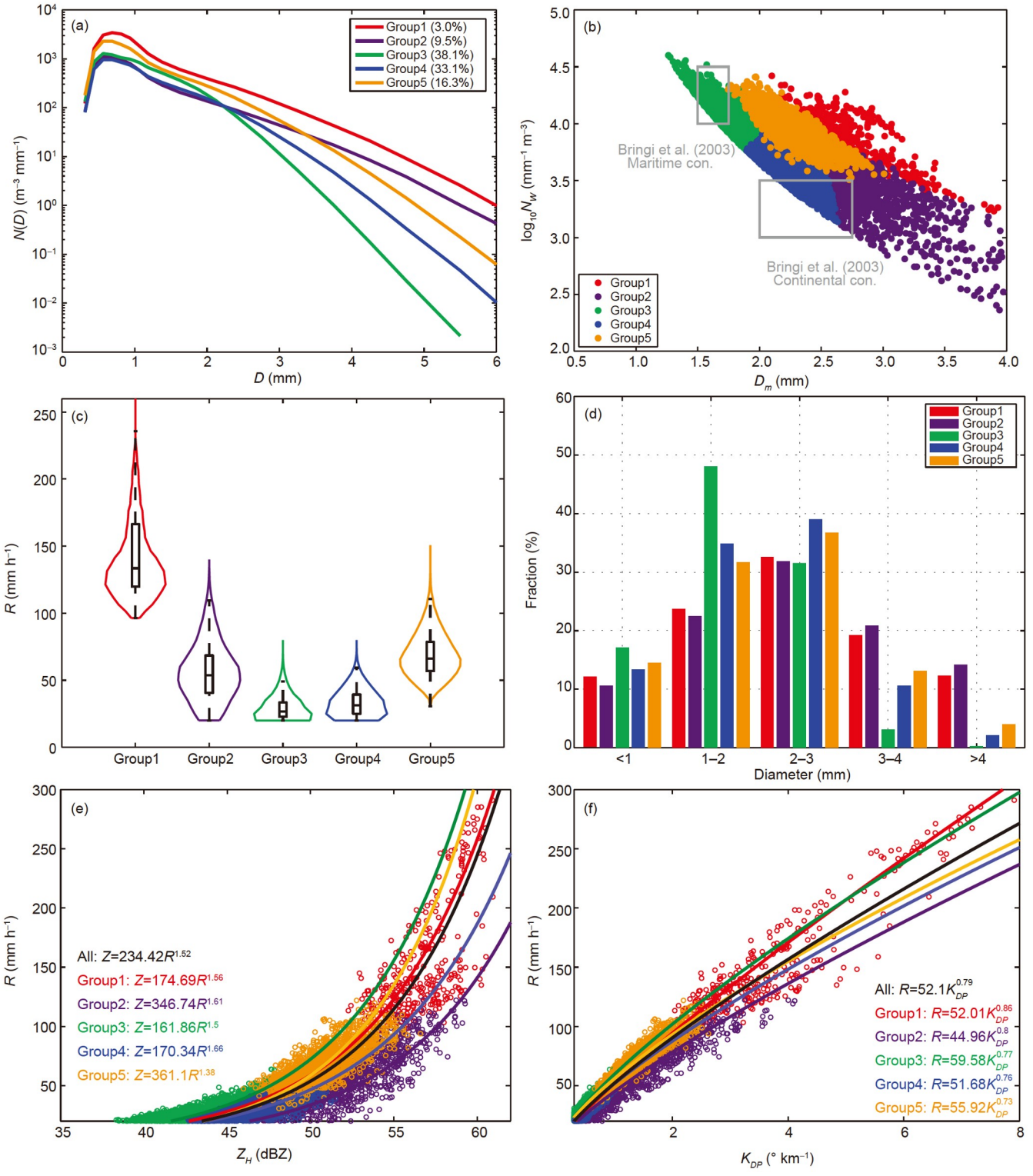

Figure 5 (a) Mean raindrop size spectra, (b) D_m-$\log_{10}(N_w)$ scatterplots, (c) rain rate boxplots, (d) relative rainfall contributions for each diameter interval to the total size ranges, (e) Z-R scatterplots and corresponding $R(Z)$ relationships, and (f) K_{DP}-R scatterplots and corresponding $R(K_{DP})$ relationships of the five DSD groups clustered with the K-means algorithm.

3×10^3 m^{-3} mm^{-1} for raindrops around 0.7 mm in group1 and was still close to 10^2 m^{-3} mm^{-1} when the raindrop diameters were 4 mm. About one-tenth of the DSD datasets (9.5%) are classified as group2 (purple), which is associated with the lowest number concentrations for small raindrops (D< 2 mm), but $N(D)$ decreased slowly when raindrop diameters

increased and possessed the second-highest number concentrations for large raindrops (D>4 mm). Conversely, the main proportion of DSD samples (38.1%) were clustered as group3 (green). Low number concentrations for large raindrops were identified in group3, but the values of $N(D)$ also exceeded 10^3 m^{-3} mm^{-1} when D<2 mm, indicating the dominant composition of small raindrops. The remaining samples were clustered into group4 (blue, 33.1%) and group5 (orange, 16.3%) with intermediate $N(D)$ values, and the raindrop number concentrations of group5 were generally higher than those of group4.

Significant distinctions are also observed within the five DSD groups from the D_m-log$_{10}$(N_w) scatterplots in Figure 5b. Samples of group1 are mainly located in the upper-right area of the entire DSD datasets, indicating both high values of mean raindrop sizes and number concentrations. The corresponding rain rates of group1 exceed 100 mm h^{-1}, with an extreme mean value of around 130 mm h^{-1} (Figure 5c). Group2 points nearly reside in the lower-right corner of the D_m-log$_{10}$(N_w) space, with values of N_w close to the typical continental convective type but with an even larger D_m. The mean rain rates of group2 are far lower than those of group1 but still exceed 50 mm h^{-1}. Conversely, the points in group3 are largely restricted to the typical maritime convective cluster area, with the overall log$_{10}$(N_w) greater than 3.5 and D_m smaller than 2 mm. Group3 also possesses the lowest mean rain rate among the five DSD groups, with dominant values below 50 mm h^{-1}. Similar values of D_m are identified in group4 and group5, which mainly range between 2.0 and 2.5 mm for the two groups. However, group5 has a higher log$_{10}$(N_w) than group4, resulting in more intense rain rates at the surface.

Relative rainfall number contributions for selected raindrop diameter intervals to total size ranges are shown in Figure 5d. Rainfall of group1 is dominantly contributed by medium raindrops, with about 50% having a diameter between 2 and 4 mm. Small raindrops (D<2 mm) contribute around 35% of rainfall, including nearly 10% for D<1 mm and 20% for D within 1–2 mm. A fraction of rainfall exceeding 10% is also provided by large raindrops (D>4 mm) in group1. The relative rainfall contributions of group2 are overall comparable to those of group1, but slightly higher (lower) fractions of raindrops larger (smaller) than 3 mm are found in group2 (group1). For group3, the primary rainfall is contributed by small raindrops, of which the peak fraction almost reaches 50% when the raindrop diameters are between 1 and 2 mm. Meanwhile, only 3% of rainfall is contributed by raindrops with diameters between 3 and 4 mm in group3, and negligible rainfall contributions are derived for large raindrops. Similar rainfall fractions are seen in group4 and group5; comparable contributions (around 30%) are found for raindrops within 1–2 and 2–3 mm, and the values are both smaller than 20% for D<1 mm and D>3 mm.

To discuss the impacts of DSD variability on QPE, the corresponding $R(Z)$ and $R(K_{DP})$ relationships of the five groups are derived in Figure 5e and 5f. The $R(Z)$ [$R(K_{DP})$] relationship is widely applied for QPE before (after) the upgrades of polarimetric radars (Fulton et al., 1997; Ryzhkov et al., 2005; Zhang, 2016). As for $R(Z)$, the best-fit equation for all heavy rainfall samples (black line) is Z=234$R^{1.52}$, which is close to the relationship obtained in eastern China for summer-time convective systems (Wen et al., 2016). However, obvious distinctions are found among the derived $R(Z)$ equations from the separate DSD groups. For a given Z_H of 50 dBZ, for example, the estimated rain rate was approximately 50 mm h^{-1} when using the fitted relationship of all samples. Much higher rainfall (nearly 80 mm h^{-1}) could be obtained when using the relationship fitted by group3, but lower rainfall (around 30 mm h^{-1}) was calculated from the relationship of group2. The maximum difference in estimated rain rates could reach 50 mm h^{-1}. The distinctions of QPE results were significantly reduced when using the fitted $R(K_{DP})$ relationships. The estimated rain rates fluctuated nearly within the 20 mm h^{-1} range when K_{DP} was 2° km^{-1}, but the range still expanded to 50 mm h^{-1} when K_{DP} was 4° km^{-1} for a tiny fraction of samples. Overall, DSD variability in this rainfall event still induces considerable difficulties in obtaining accurate QPE results when using the single fitted $R(K_{DP})$ equation.

3.4 Microphysical structures of varied DSD groups

Observations of two S-band polarimetric radars (ZZRD and LYRD) are also analyzed in the study to further investigate the vertical microphysical structures contributing to the surface DSDs in each group. Vertical radar variables and identified hydrometeor species over the OTT disdrometers are selected as follows. For each OTT at a given location, the corresponding distances to the two polarimetric radars were first calculated. Only a radar 20–120 km away from the disdrometer is selected for use in the analysis. If both radars meet the distance requirements, datasets from the closer radar are used. Then, the closest radar VCP in time match with each OTT heavy rainfall sample is determined, and datasets within a 3-km×3-km area centered on the OTT station are picked out for the analysis. This setup is unideal due to the inconsistency of temporal and spatial resolutions between the two types of instruments, but the uncertainties can be reduced when comparing the overall mean values of statistical observations.

The average Z_H, Z_{DR}, and K_{DP} profiles of the five DSD groups are presented in Figure 6. Significantly distinct signatures are identified in group1 (red) compared with the other four groups from the profiles. The largest mean Z_H values are found throughout all latitudes in group1, and the mean height of 30-dBZ echo reaches 8 km and is higher than

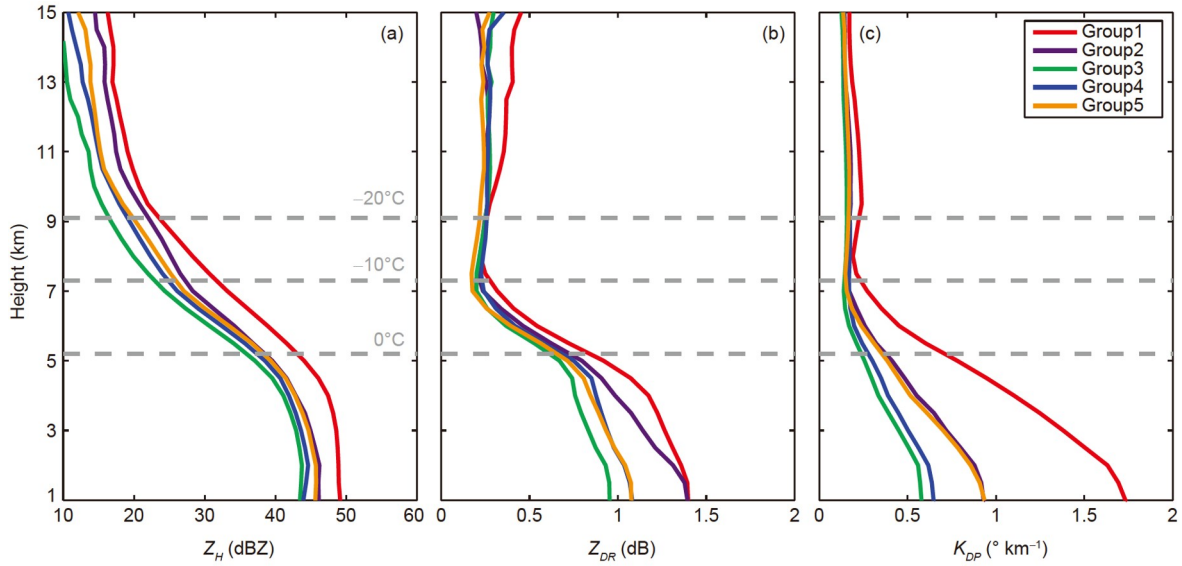

Figure 6 The average profiles of (a) Z_H, (b) Z_{DR}, and (c) K_{DP} correspond to the five DSD groups from polarimetric radar observations. The 0, −10 and −20°C levels from radiosonde observations are denoted by the gray dashed lines from bottom to top.

the −10°C level, suggesting deep convection with intense updrafts (DeMott and Rutledge, 1998). Group1 also possesses the highest Z_{DR} and K_{DP} values below the −10°C level, where the mean Z_{DR} is around 0.3 dB at the −10°C level and persistently increases to 1.3 dB at the 4-km AGL, and then slowly raises to 1.4 dB toward the 1-km level (Figure 6b). We suggest that the greatest Z_{DR} above the freezing levels is primarily contributed by supercooled raindrops transported by the strongest updrafts (Rowe et al., 2011; Wang et al., 2016) because the ice particles of snow and graupel are generally regarded as spherical hydrometeors, and their Z_{DR} values are close to 0 dB (Dolan et al., 2013; Friedrich et al., 2016). The downward increase in Z_{DR} from the freezing level to the 4-km AGL is attributed to the melting of large-sized ice hydrometeors, the further growth of Z_{DR} values within the warm cloud layers indicates the active collision-coalescence processes (Kumjian and Prat, 2014). For K_{DP}, the related mean value increases continuously from 0.3° km^{-1} at the −10°C level to nearly 1.7° km^{-1} at the 1-km AGL (Figure 6c). Because K_{DP} is partially related to the LWC (Zrnić and Ryzhkov, 1996), it also indicates the transport of liquid hydrometeors through strong updrafts above the freezing level and efficient collision-coalescence processes within the warm cloud layers (Kumjian and Prat, 2014; Chen et al., 2019). Based on the average radar profiles of group1, the extreme surface rainfall is generally contributed by deep convection with both active ice-phase and warm-rain processes.

Group3 (green) has the lowest mean Z_H values for all latitudes (Figure 6a), with a height of 30-dBZ echo only around 6 km. The mean Z_H of group3 at the −20°C level is at least 5 dB lower than that of the other four groups, indicating a designation of the shallowest convection and likely the weakest vertical motions (Friedrich et al., 2016). Both the lowest values of Z_{DR} and K_{DP} throughout the warm cloud layers are observed in group3, suggesting the smallest mean size of raindrops and a relatively low LWC. However, the mean polarimetric radar variables continuously increased below the freezing level in this group, indicating the majority contribution of surface rainfall by efficient collision-coalescence processes (Carr et al., 2017). Another distinctive feature comes from group2 (purple), the mean Z_H and K_{DP} values are overall lower than those of group1 spanned over all vertical layers, suggesting that shallower convection contains lower LWC. Meanwhile, the mean value of group2 Z_{DR} was approximately 0.3 dB lower than that of group1 at the 4-km level, but increased faster for the former group, leading to a comparable Z_{DR} value of the two groups at the 1-km AGL. Z_{DR} is a typical indicator for raindrop mean size within the warm cloud layers, its anomalous value growth also reflects the increase of mean raindrop diameters through collision-coalescence processes (Kumjian and Prat, 2014). Comparative Z_{DR} profiles are also identified between group4 (blue) and group5 (orange), although about 1 dBZ higher Z_H values are observed at low levels for the latter group. The growth of K_{DP} values within the warm cloud layers is also faster for group5 than group4, with an approximately 0.3° km^{-1} gap at the 1-km AGL, suggesting more efficient collision-coalescence processes in group5 (Carr et al., 2017). Results between group4 and group5 are consistent with the DSD characteristics in Figure 5. Similar D_m values for the two groups are consistent with the comparable Z_{DR} values, but higher raindrop number concentrations for group5 correspond to higher mean rain rate, Z_H, and K_{DP} values.

Occurrence fractions of the identified hydrometeors in vertical layers for each DSD group are shown in Figure 7.

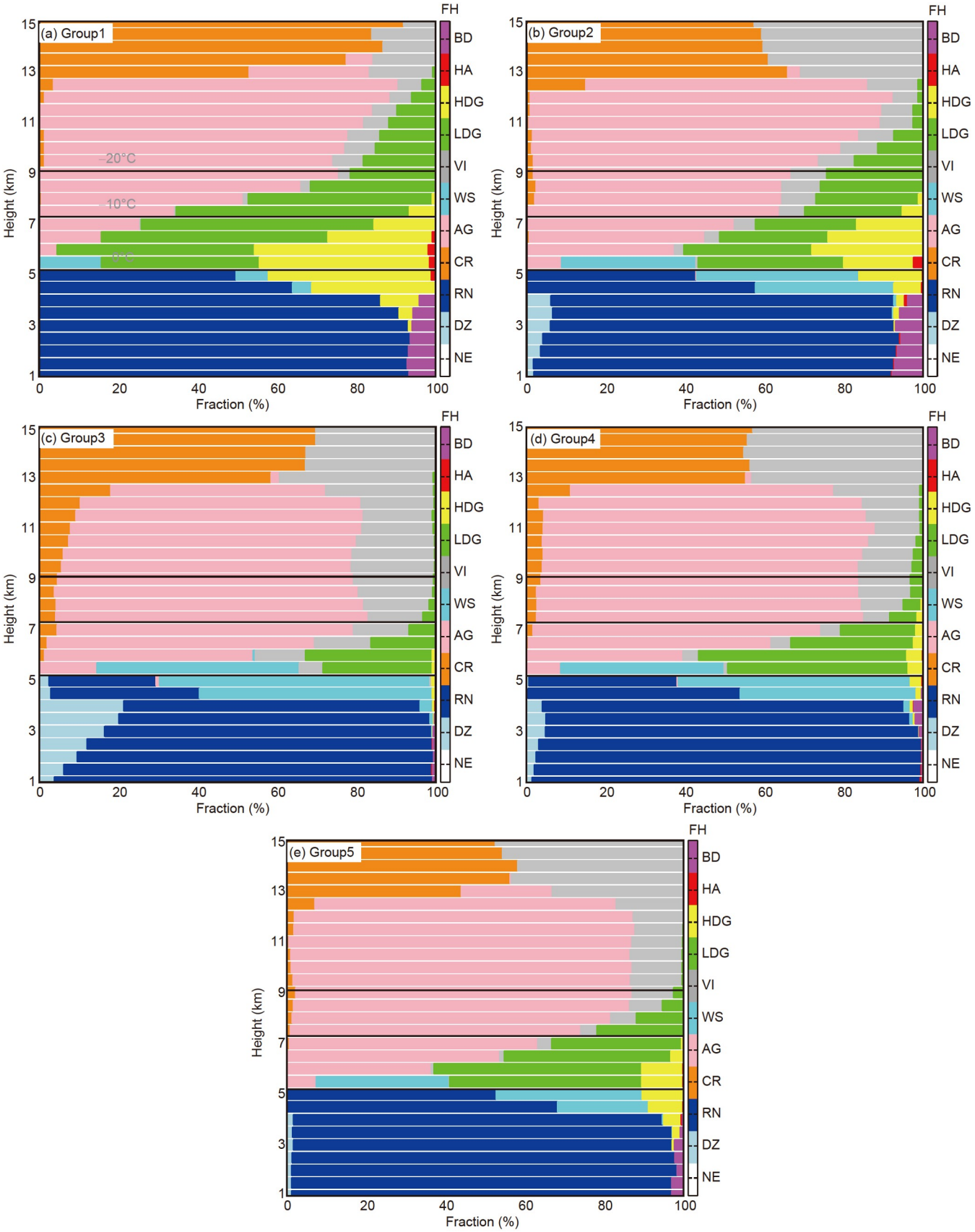

Figure 7 Occurrence fractions of identified hydrometeors in vertical layers for each DSD group.

For 10 types of identified hydrometeors, their occurrence number fractions compared with total samples at each 0.5-km radar vertical gird layer are obtained. The statistical analysis helps reduce the uncertainties of the HID algorithm and provides the overall dominant hydrometeor type in certain vertical layers (Chen et al., 2019; Friedrich et al., 2016). Group1 possesses the highest graupel fractions (yellow for HDG and green for LDG) above the freezing level, where the maximum value is almost 100% at the 6-km AGL and still shares a 10% number fraction at around the 11-km AGL. The mean graupel fraction is around 80% between the −10°C and freezing levels (Figure 7a), indicating active riming processes in the adequately mixed region of falling ice particles and uploaded liquid hydrometeors (Barnes and Houze, 2014; Homeyer and Kumjian, 2015). After the melting of graupel in group1, the dominant raindrops (around 95%) and a small proportion of big drops (5%) are identified below the 4-km AGL.

The second-highest graupel occurrence frequencies are found in group2 (Figure 7b), with a fraction of 10% around the 10-km AGL and a peak value of 60% at the 6-km level. Active ice-phase processes also occur in the convection of group2, and almost equivalent fractions of big drops are identified at low levels compared with group1. Meanwhile, the minimum quantities of graupel exist in group3, where the dominant hydrometeor species is snow between the −20°C and freezing levels. For this reason, negligible big drops are formed from the melting of large ice particles at low levels, and the smallest D_m is observed at the surface (Figure 5b). Moderate vertical graupel fractions are identified in group4 and group5. Slightly higher graupel fractions are found in group5, which is related to higher raindrop concentrations and rain rates of the DSD group at the surface.

3.5 Spatial distribution of DSD groups

Based on the above analysis above, the surface DSD variability is derived from the distinct precipitation structures and inferred microphysical process activations along the vertical axis. There is another remaining question, whether the clustered DSDs have particularly spatial distribution characteristics? Therefore, the occurrence distributions of the five DSD groups in the dense OTT network are further investigated. For each of the top five OTT stations with the most frequent samples belonging to the clustered DSD groups, their spatial distributions during different periods are shown in Figure 8. Owing to the disparity of rainfall accumulations at different OTT stations, it is unfair to directly compare the observed sample quantities of certain DSD groups. To reduce uncertainties, the relative fractions of each DSD group to total samples at individual OTT stations are first calculated, and the five stations (10% of 50 OTTs) with the top fraction values are then selected and labeled in the figure.

During the entire analysis period, from July 19 to 21, the "typical" (top five fractions) group3 OTT stations (green) are clustered near the 500-m terrain height contours (black line) (Figure 8a). The stations possess maritime-like convective DSDs with high (low) concentrations of small (large) raindrops, one of which (53984) is shown in Figure 4a. Conversely, the "typical" group1 stations (red) are mainly located in regions away from the 500-m terrain contours, three of which [57083 (ZZ), 57091, and 57098] are illustrated in Figure 4. Although there is some inconsistency, most "typical" group2 stations (purple) are also found to be located at some distance from the orographic regions, two of which are coincident with group1 stations. Moreover, the "typical" stations are mainly found nearby orographic regions for group4 and mainly distributed in plain regions for group5 (orange), and with a certain degree of location dispersions. Together, it is likely that the DSD groups with relatively lower (higher) rain rates and D_m values are easier to form in the regions nearby orographic regions (plain), consistent with the findings in previous studies (Lang et al., 2009; Houze, 2012; Xu, 2013; Zagrodnik et al., 2019). Similar distributions of the "typical" stations have also been obtained for individual days (Figure 8b–8d); the "typical" group3 stations always seem to be located nearby orography, whereas the "typical" group1 and group2 stations majorly distribute over the plain regions. Besides, the "typical" stations of all DSD groups were mainly located around Zhengzhou on July 19 but shifted eastward on July 20, and several "typical" group1 and group2 stations further moved to the north on July 21. The movements of these "typical" stations agree with the development of precipitation systems during the 3-day period and indicate the evolution of synoptic conditions (Ran et al., 2021; Su et al., 2021).

To further compare the precipitation structures under different topographic conditions with different types of "typical" DSD stations, average profiles of polarimetric radar variables in two selected regions are presented in Figure 9. One of the regions is mainly distributed near the orography (named "Region T") and covers all "typical" group3 OTT stations from July 19 to 21, as is outlined by the gray rectangle in Figure 8a. The other region is away from the 500-m terrain contours (named "Region P") and contains three (two) "typical" OTT stations of group1 (group2). Datasets within the rectangles are selected from the closer polarimetric radar-observed VCPs during the 3-day period, the same as in Figure 6. The standard deviations of the radar variables in each altitude layer are also outlined by the corresponding error bars.

Significant distinctions are found in the average radar profiles of the two regions. The Z_H values of Region P (orange) are nearly 10 dB higher than those of Region T (blue) above the −10°C level, indicating much deeper convection

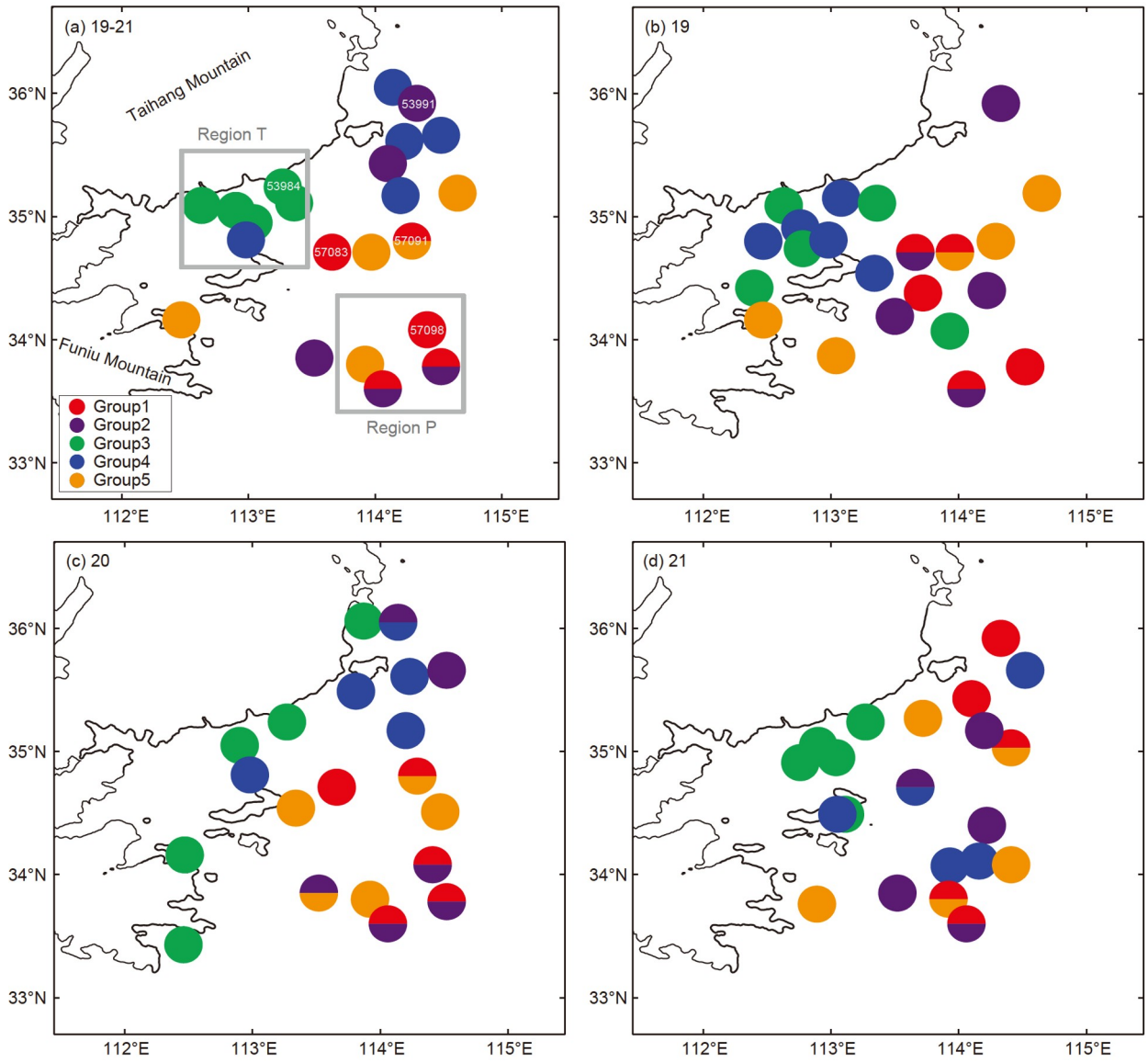

Figure 8 Spatial distributions of five most frequent occurrence OTT stations for individual DSD groups during (a) July 19–21, (b) July 19, (c) July 20, and (d) July 21. Stations labeled with two colors represent the frequent occurrence of two DSD groups. The 500-m terrain height contours are denoted with black lines. Station IDs of the selected disdrometers in Figure 4a–4f are marked in Figure 8a; two selected regions for further comparison are also outlined with gray rectangles.

from the former region. Smaller standard deviations of Z_{DR} values are also found in Region P at these altitude layers, attributable to the widespread snow particles (smaller Z_{DR} ranges) but low fractions of ice crystals (larger Z_{DR} ranges) there (Andrić et al., 2013; Schrom and Kumjian, 2018). More rapid increases in Z_{DR} and K_{DP} values are also found from the −10°C level to the freezing level in Region P, suggesting higher contents of liquid particles supplied by stronger updrafts. Moreover, gaps in the mean Z_H and K_{DP} values in the two regions gradually decrease from the freezing level to the 1-km AGL; hence, it is very likely that a more efficient collision-a coalescence of raindrops exists within the warm cloud layers of Region T (Kumjian and Prat, 2014; Carr et al., 2017). Region P also has higher mean Z_{DR} values below the freezing level, indicating the formation of larger raindrops through the melting of large ice particles such as graupel. Higher (lower) graupel fractions are also found in Region P from HID retrievals (not shown), which agree with the inferred analysis from the radar variable profiles. Finally, larger standard deviations of the radar variables, especially for K_{DP}, exist in Region P within the warm cloud layers, indicating the composition of more complicated precipitation types related to the multiple surface DSD groups.

4. Discussions and conclusions

In this study, we examine the variability of microphysical

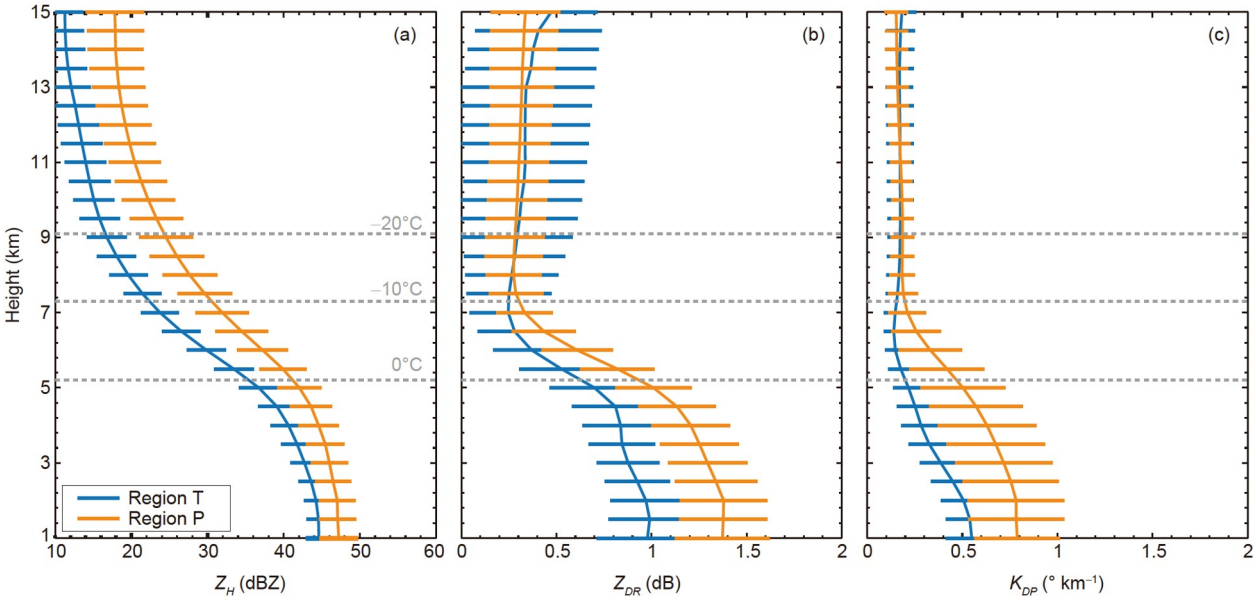

Figure 9 Comparison of (a) Z_H, (b) Z_{DR}, and (c) K_{DP} average profiles for the two selected regions in Figure 8a. Error bars denote the standard deviation in each altitude layer. The 0, −10 and −20°C levels are also outlined by the gray dashed lines, as in Figure 6.

characteristics in the "21·7" Henan EHR event from the combined observations of a dense network of disdrometers and two polarimetric radars. Majority of the extreme precipitation is produced for a 3-day period from July 19 to 21 2021; obvious DSD variability is derived from all heavy rainfall samples of 50 OTT disdrometers. The OTT data are clustered into five groups using the K-means clustering algorithm, and distinct DSD characteristics are obtained among the DSD groups. Vertical structures of the DSD groups are compared through the observations of the polarimetric radars, and the distinctions of microphysical structures causing the surface DSD variability are investigated. The spatial distributions of the DSD groups are also discussed.

The extreme rainfall is generally captured by the dense network of OTT disdrometers operated by CMA. D_m-$\log_{10}(N_w)$ values are widely distributed from the typical maritime convective clusters to the continental convective area reported by Bringi et al. (2003), indicating significant microphysical variability. To quantitatively describe the microphysical variability, the OTT datasets are objectively clustered into five groups by a K-means clustering algorithm, and distinctive rain rates, D-$\log_{10}[N(D)]$, D_m-$\log_{10}(N_w)$, and rainfall contributions of raindrop sizes are obtained among the five DSD groups. Group1 is characterized by extreme rain rates and high concentrations of raindrops in the entire size range. Group2 is identified with the largest raindrop mean sizes but the lowest concentrations of small raindrops. The D_m-$\log_{10}(N_w)$ distributions of group3 are majorly restricted to the typical maritime convective area, with negligible large raindrops observed. Values of D_m-$\log_{10}(N_w)$ are majorly distributed in the middle of typical maritime and continental convective clusters in group4 and group5, and higher raindrop number concentrations are found in group5, resulting in more intense rain rates. Because of the DSD variability, huge distinctions in QPE results are obtained from the R(Z) relationships fitted from the separate DSD groups. Although the inconsistency in QPE results is reduced by the R(K_{DP}) relations, DSD variability still induces considerable difficulties in obtaining accurate precipitation amounts from the single QPE relationship.

Microphysical structures over the OTT stations are provided by the supporting observations of the two polarimetric radars. The highest values of averaged Z_H are obtained throughout all vertical latitudes in group1, and the most abundant graupel are equally identified above the freezing level, indicating the existence of deep convection with active ice-phase processes. Persistent increases in K_{DP} are also found within the warm cloud layers of group1, suggesting potentially efficient warm-rain coalescence of raindrops. The very distinctive precipitation structures are identified in group3, where the lowest radar echo heights reflect the shallowest convection with limited riming processes. Surface DSDs are mainly determined by the active warm-rain processes. Group2 is also indicated by high Z_{DR} values accompanied by moderate Z_H and K_{DP} among the DSD groups. Moreover, group3 is found to be primarily distributed near the orographic regions, whereas clusters corresponding to deeper convection (group1 and group2) are more easily formed near the plain. Microphysical variability is likely to be related to topographic conditions from the comparison of radar variable profiles in two areas with different terrain heights. All DSD groups are found to coexist in the lowlands, indicating potential microphysical variability within the deep

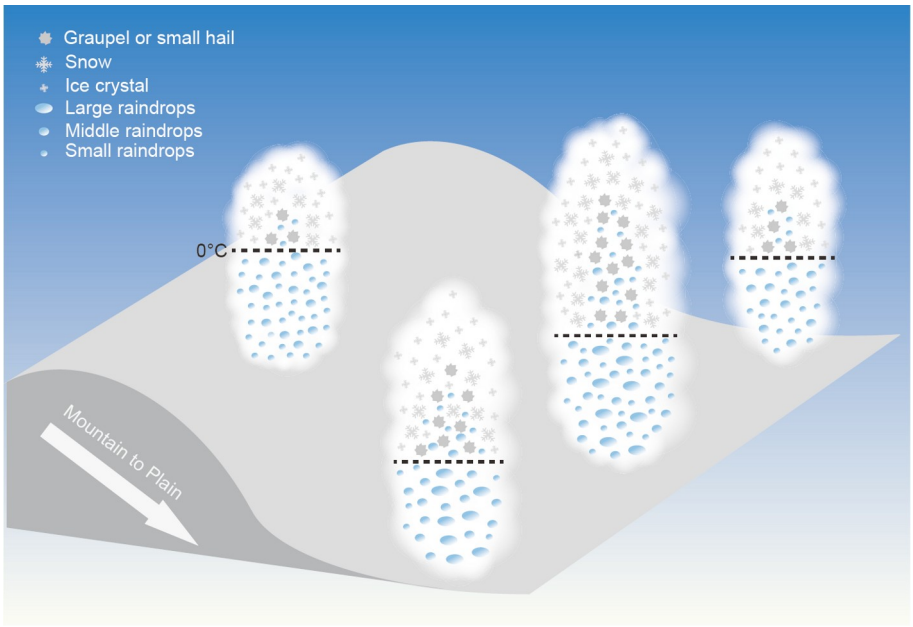

Figure 10 Conceptual model illustrating the microphysical variability in the "21·7" EHR event based on disdrometer and polarimetric radar observations. Convection is relatively deeper (shallower) over the plain (mountain) regions, with ice particles (graupel, snow, and ice crystal) distributed throughout higher (lower) vertical layers above the freezing level. Surface rainfall near orographic regions is dominantly contributed by the high-concentration and small raindrops produced by efficient warm-rain processes. Obvious microphysical variability is also found in the convection near the plain; concentrations and sizes of surface raindrops change along with the variation in convection depths. Extreme surface rainfall is only formed in the deep mature convection, where abundant raindrops of various sizes are produced through both active ice-phase and warm-rain processes.

convection. A simplified conceptual model is provided in Figure 10 to summarize the possible microphysical variability in the convection of this extreme rainfall event.

Although the complexity of precipitation microphysics in the "21·7" Henan EHR event is preliminarily revealed in this study, more analysis should be performed. For example, the convective/mesoscale dynamics and microphysical processes that generate record-breaking hourly rainfall (201.9 mm) in Zhengzhou can be further examined using three-dimensional wind and thermodynamic and microphysical fields obtained from an advanced radar data assimilation system. Additionally, more accurate QPE estimators can be established by considering the DSD variability. To discuss the possible influences on QPF performance, the capability to reproduce the microphysical variability in a model should also be evaluated in the future. We also suggest designing more customized observation strategies by combining the existing in situ instruments and remote-sensing measurements to obtain the comprehensive structures of severe storms. Besides, certain quantities of super observation stations should be constructed in regions with frequent meteorological hazards. The combined observations of microwave radiometer, cloud-aerosol lidar, multifrequency vertically pointing radars and disdrometers at the same site will help elucidate the formation of raindrops through complete growth processes.

Acknowledgements *We would like to acknowledge the China Meteorological Administration for collecting and archiving the disdrometer, rain gauge and radiosonde data used in this study. This work was jointly supported by the National Natural Science Foundation of China (Grant Nos. 42025501, 42005009, 41875053, U2142203), the National Key Research and Development Program of China (Grant No. 2017YFC1501703), the Basic Research Fund of CAMS (Grant No. 2021Z003) and the Open Research Program of the State Key Laboratory of Severe Weather (Grant No. 2020LASW-A01).*

References

Anderberg M R. 2014. Cluster Analysis for Applications: Probability and Mathematical Statistics: A Series of Monographs and Textbooks. London: Academic Press. 19

Andrić J, Kumjian M R, Zrnić D S, Straka J M, Melnikov V M. 2013. Polarimetric Signatures above the melting layer in winter storms: An observational and modeling study. J Appl Meteorol Climatol, 52: 682–700

Bang W, Lee G W, Ryzhkov A, Schuur T, Sunny Lim K S. 2020. Comparison of microphysical characteristics between the Southern Korean Peninsula and Oklahoma using two-dimensional video disdrometer data. J Hydrometeorol, 21: 2675–2690

Bao X, Wu L, Zhang S, Li Q, Lin L, Zhao B, Wu D, Xia W, Xu B. 2020. Distinct raindrop size distributions of convective inner- and outer-rainband rain in Typhoon Maria (2018). J Geophys Res-Atmos, 125: e32482

Barnes H C, Houze Jr. R A. 2014. Precipitation hydrometeor type relative to the mesoscale airflow in mature oceanic deep convection of the Madden-Julian Oscillation. J Geophys Res-Atmos, 119: 13,990–14,014

Brandes E A, Zhang G, Vivekanandan J. 2002. Experiments in rainfall estimation with a polarimetric radar in a subtropical environment. J Appl Meteorol, 41: 674–685

Bringi V N, Rasmussen R M, Vivekanandan J. 1986. Multiparameter radar measurements in Colorado convective storms. Part I: Graupel melting studies. J Atmos Sci, 43: 2545–2563

Bringi V N, Chandrasekar V, Hubbert J, Gorgucci E, Randeu W L, Schoenhuber M. 2003. Raindrop size distribution in different climatic regimes from disdrometer and dual-polarized radar analysis. J Atmos Sci, 60: 354–365
Brown B R, Bell M M, Frambach A J. 2016. Validation of simulated hurricane drop size distributions using polarimetric radar. Geophys Res Lett, 43: 910–917
Carr N, Kirstetter P E, Gourley J J, Hong Y. 2017. Polarimetric signatures of midlatitude warm-rain precipitation events. J Appl Meteorol Climatol, 56: 697–711
Chang W Y, Lee W C, Liou Y C. 2015. The kinematic and microphysical characteristics and associated precipitation efficiency of subtropical convection during SoWMEX/TiMREX. Mon Weather Rev, 143: 317–340
Chen B, Wang J, Gong D. 2016. Raindrop size distribution in a midlatitude continental squall line measured by thies optical disdrometers over East China. J Appl Meteorol Climatol, 55: 621–634
Chen B, Yang J, Gao R, Zhu K, Zou C, Gong Y, Zhang R. 2020. Vertical variability of the raindrop size distribution in typhoons observed at the Shenzhen 356-m meteorological tower. J Atmos Sci, 77: 4171–4187
Chen G, Zhao K, Huang H, Yang Z, Lu Y, Yang J. 2021. Evaluating Simulated Raindrop Size Distributions and Ice Microphysical Processes With Polarimetric Radar Observations in a Meiyu Front Event Over Eastern China. J Geophys Res, 126: E2020JD034511
Chen G, Zhao K, Wen L, Wang M, Huang H, Wang M, Yang Z, Zhang G, Zhang P, Lee W C. 2019. Microphysical characteristics of three convective events with intense rainfall observed by polarimetric radar and disdrometer in Eastern China. Remote Sens, 11: 2004–2023
Chen G, Zhao K, Zhang G, Huang H, Liu S, Wen L, Yang Z, Yang Z, Xu L, Zhu W. 2017. Improving polarimetric C-band radar rainfall estimation with two-dimensional video disdrometer observations in Eastern China. J Hydrometeorol, 18: 1375–1391
Cifelli R, Chandrasekar V, Chen H, Johnson L E. 2018. High resolution radar quantitative precipitation estimation in the San Francisco Bay Area: Rainfall monitoring for the urban environment. J Meteorol Soc Jpn, 96A: 141–155
DeMott C A, Rutledge S A. 1998. The vertical structure of TOGA COARE convection. Part I: Radar echo distributions. J Atmos Sci, 55: 2730–2747
DeHart J C, Bell M M. 2020. A comparison of the polarimetric radar characteristics of heavy rainfall from Hurricanes Harvey (2017) and Florence (2018). J Geophys Res-Atmos, 125: e2019JD032212
Dolan B, Fuchs B, Rutledge S A, Barnes E A, Thompson E J. 2018. Primary modes of global drop size distributions. J Atmos Sci, 75: 1453–1476
Dolan B, Rutledge S A, Lim S, Chandrasekar V, Thurai M. 2013. A robust C-band hydrometeor identification algorithm and application to a long-term polarimetric radar dataset. J Appl Meteorol Climatol, 52: 2162–2186
Friedrich K, Higgins S, Masters F J, Lopez C R. 2013. Articulating and stationary PARSIVEL disdrometer measurements in conditions with strong winds and heavy rainfall. J Atmos Ocean Tech, 30: 2063–2080
Friedrich K, Kalina E A, Aikins J, Gochis D, Rasmussen R. 2016. Precipitation and cloud structures of intense rain during the 2013 great Colorado flood. J Hydrometeorol, 17: 27–52
Friedrich K, Kalina E A, Aikins J, Steiner M, Gochis D, Kucera P A, Ikeda K, Sun J. 2015. Raindrop size distribution and rain characteristics during the 2013 great Colorado flood. J Hydrometeorol, 17: 53–72
Fulton R A, Breidenbach J P, Seo D J, Miller D A, O'Bannon T. 1997. The WSR-88D rainfall algorithm. Weather Forecast, 13: 377–395
Giangrande S E, Ryzhkov A V. 2005. Calibration of dual-polarization radar in the presence of partial beam blockage. J Atmos Ocean Tech, 22: 1156–1166
Giangrande S E, Ryzhkov A V. 2009. Estimation of Rainfall Based on the Results of Polarimetric Echo Classification. J Appl Meteorol Clim, 48: 690–690
Han B, Du Y, Wu C, Liu X. 2021. Microphysical characteristics of the coexisting frontal and warm-sector heavy rainfall in South China. J Geophys Res-Atmos, 126: e35446
Hartigan J A, Wong M A. 1979. Algorithm AS 136: A K-means clustering algorithm. Appl Stat, 28: 100
Homeyer C R, Kumjian M R. 2015. Microphysical characteristics of overshooting convection from polarimetric radar observations. J Atmos Sci, 72: 870–891
Houze R A. 2012. Orographic effects on precipitating clouds. Rev Geophys, 50: RG1001
Huang H, Zhao K, Zhang G, Lin Q, Wen L, Chen G, Yang Z, Wang M, Hu D. 2018. Quantitative precipitation estimation with operational polarimetric radar measurements in Southern China: A differential phase-based variational approach. J Atmos Ocean Tech, 35: 1253–1271
Kumjian M R, Prat O P. 2014. The impact of raindrop collisional processes on the polarimetric radar variables. J Atmos Sci, 71: 3052–3067
Lang T J, Rutledge S A, Cifelli R. 2009. Polarimetric radar observations of convection in northwestern Mexico during the North American Monsoon Experiment. J Hydrometeorol, 11: 1345–1357
Löffler-Mang M, Joss J. 2000. An optical disdrometer for measuring size and velocity of hydrometeors. J Atmos Ocean Technol, 17: 130–139
Luo Y, Zhang R, Qian W, Luo Z, Hu X. 2011. Intercomparison of deep convection over the Tibetan Plateau-Asian monsoon region and subtropical North America in boreal summer using CloudSat/CALIPSO data. J Clim, 24: 2164–2177
Markowski P, Richardson Y. 2010. Mesoscale Meteorology in Midlatitudes. Hoboken: John Wiley & Sons. 206
Matrosov S Y, Cifelli R, Neiman P J, White A B. 2016. Radar rain-rate estimators and their variability due to rainfall type: An assessment based on hydrometeorology testbed data from the Southeastern United States. J Appl Meteorol Climatol, 55: 1345–1358
Putnam B J, Xue M, Jung Y, Zhang G, Kong F. 2016. Simulation of polarimetric radar variables from 2013 CAPS spring experiment storm-scale ensemble forecasts and evaluation of microphysics schemes. Mon Weather Rev, 145: 49–73
Ran L, Li S, Zhou Y, Yang S, Ma S, Zhou K, Shen D, Jiao B, Li N. 2021. Observational analysis of the dynamic, thermal, and water vapor characteristics of the "7.20" extreme rainstorm event in Henan Province (in Chinese). Chin J Atmos Sci, 45: 1366–1383
Raut B A, Konwar M, Murugavel P, Kadge D, Gurnule D, Sayyed I, Todekar K, Malap N, Bankar S, Prabhakaran T. 2021. Microphysical origin of raindrop size distributions during the Indian monsoon. Geophys Res Lett, 48: e93581
Rowe A K, Rutledge S A, Lang T J. 2011. Investigation of microphysical processes occurring in isolated convection during NAME. Mon Weather Rev, 139: 424–443
Ryu J, Song H J, Sohn B J, Liu C. 2021. Global distribution of three types of drop size distribution representing heavy rainfall from GPM/DPR measurements. Geophys Res Lett, 48: e90871
Ryzhkov A V, Giangrande S E, Schuur T J. 2005. Rainfall estimation with a polarimetric prototype of WSR-88D. J Appl Meteorol, 44: 502–515
Schrom R S, Kumjian M R. 2018. Bulk-density representations of branched planar ice crystals: Errors in the polarimetric radar variables. J Appl Meteorol Climatol, 57: 333–346
Seela B K, Janapati J, Lin P L, Reddy K K, Shirooka R, Wang P K. 2017. A comparison study of summer season raindrop size distribution between Palau and Taiwan, two islands in Western Pacific. J Geophys Res-Atmos, 122: 11,787–11,805
Shi W, Li X, Zeng M, Zhang B, Wang H, Zhu K, Zhuge X. 2021. Multi-model comparison and high-resolution regional model forecast analysis for the "7·20" Zhengzhou severe heavy rain (in Chinese). Trans Atmos Sci, 44: 688–702
Su A, Lu X, Cui L, Li Z, Xi L, Su H. 2021. The basic observational analysis of "7.20" extreme rainstorm in Zhengzhou (in Chinese). Torr Rain Disast, 40: 445–454
Thompson E J, Rutledge S A, Dolan B, Thurai M. 2015. Drop size distributions and radar observations of convective and stratiform rain over the equatorial Indian and West Pacific Oceans. J Atmos Sci, 72: 4091–

4125
Vivekanandan J, Ellis S M, Oye R, Zrnic D S, Ryzhkov A V, Straka J. 1999. Cloud microphysics retrieval using S-band dual-polarization radar measurements. Bull Amer Meteorol Soc, 80: 381–388
Wang M, Zhao K, Pan Y, Xue M. 2020. Evaluation of simulated drop size distributions and microphysical processes using polarimetric radar observations for landfalling Typhoon Matmo (2014). J Geophys Res-Atmos, 125: e31527
Wang M, Zhao K, Xue M, Zhang G, Liu S, Wen L, Chen G. 2016. Precipitation microphysics characteristics of a Typhoon Matmo (2014) rainband after landfall over eastern China based on polarimetric radar observations. J Geophys Res-Atmos, 121: 12,415–12,433
Wen J, Zhao K, Huang H, Zhou B, Yang Z, Chen G, Wang M, Wen L, Dai H, Xu L, Liu S, Zhang G, Lee W C. 2017. Evolution of microphysical structure of a subtropical squall line observed by a polarimetric radar and a disdrometer during OPACC in Eastern China. J Geophys Res-Atmos, 122: 8033–8050
Wen L, Zhao K, Chen G, Wang M, Zhou B, Huang H, Hu D, Lee W C, Hu H. 2018. Drop size distribution characteristics of seven Typhoons in China. J Geophys Res-Atmos, 123: 6529–6548
Wen L, Zhao K, Yang Z, Chen H, Huang H, Chen G, Yang Z. 2020. Microphysics of stratiform and convective precipitation during meiyu season in Eastern China. J Geophys Res-Atmos, 125: e32677
Wen L, Zhao K, Zhang G, Liu S, Chen G. 2017. Impacts of instrument limitations on estimated raindrop size distribution, radar parameters, and model microphysics during Mei-Yu season in East China. J Atmos Ocean Tech, 34: 1021–1037
Wen L, Zhao K, Zhang G, Xue M, Zhou B, Liu S, Chen X. 2016. Statistical characteristics of raindrop size distributions observed in East China during the Asian summer monsoon season using 2-D video disdrometer and Micro Rain Radar data. J Geophys Res-Atmos, 121: 2265–2282
Wu D, Zhao K, Kumjian M R, Chen X, Huang H, Wang M, Didlake Anthony C. J, Duan Y, Zhang F. 2018. Kinematics and microphysics of convection in the outer rainband of Typhoon Nida (2016) revealed by polarimetric radar. Mon Weather Rev, 146: 2147–2159
Xu W. 2013. Precipitation and convective characteristics of summer deep convection over East Asia observed by TRMM. Mon Weather Rev, 141: 1577–1592
Yin J, Gu H, Liang X, Yu M, Sun J, Xie Y, Li F, Wu C. 2021. A Possible Dynamic Mechanism for Rapid Production of the Extreme Hourly Rainfall in Zhengzhou City on 20 July 2021. J Meteorol Res, 36: 1–20
Zagrodnik J P, McMurdie L A, Houze Robert A. J, Tanelli S. 2019. Vertical structure and microphysical characteristics of frontal systems passing over a three-dimensional coastal mountain range. J Atmos Sci, 76: 1521–1546
Zeng Q, Zhang Y, Lei H, Xie Y, Gao T, Zhang L, Wang C, Huang Y. 2019. Microphysical Characteristics of Precipitation during Pre-monsoon, Monsoon, and Post-monsoon Periods over the South China Sea. Adv Atmos Sci, 36: 1103–1120
Zhang G. 2016. Weather Radar Polarimetry. Boca Raton (FL): CRC Press
Zhang G, Vivekanandan J, Brandes E. 2001. A method for estimating rain rate and drop size distribution from polarimetric radar measurements. IEEE Trans Geosci Remote Sens, 39: 830–841
Zhang X, Yang H, Wang X, Shen L, Wang D, Su H. 2021. Analysis on characteristic and abnormality of atmospheric circulations of the July 2021 extreme precipitation in Henan (in Chinese). Trans Atmos Sci, 44: 672–687
Zhao K, Huang H, Wang M, Lee W C, Chen G, Wen L, Wen J, Zhang G, Xue M, Yang Z, Liu L, Wu C, Hu Z, Chen S. 2019. Recent progress in dual-polarization radar research and applications in China. Adv Atmos Sci, 36: 961–974
Zrnić D S, Ryzhkov A. 1996. Advantages of rain measurements using specific differential phase. J Atmos Ocean Technol, 13: 454–464

(Responsible editor: Zhiyong MENG)